Vertically Aligned Two-Dimensional Graphene-Metal Hydroxide Hybrid Arrays for Li–O$_2$ Batteries

Abstract

Lithium oxygen batteries (LOBs) are a very promising upcoming technology which, however, still suffers from low lifespan and dramatic capacities fading. Solid discharge products increase the contact resistance and block the electrochemically active electrodes. The resulting high oxidative potentials and formation of Li$_2$CO$_3$ due to electrolyte and carbon electrode decomposition at the positive electrode lead to irreversible deactivation of oxygen evolution reaction (OER) and oxygen reduction reaction (ORR) sites. Here we demonstrate a facile strategy for the scalable production of a new electrode structure constituted of vertically aligned carbon nanosheets and metal hydroxide (M(OH)$_x$@CNS) hybrid arrays, integrating both favorable ORR and OER active materials to construct bifunctional catalysts for LOBs. Excellent lithium–oxygen battery properties with high specific capacity of 5403 mAh g^{-1} and 12123 mAh g^{-1} referenced to the carbon and M(OH)$_x$ weight, respectively, long cyclability, and low charge potentials are achieved in the resulting M(OH)$_x$@CNS cathode architecture. The properties are explained by improved O$_2$/ion transport properties and spatially limited precipitation of Li$_2$O$_2$ nanoparticles inside interstitial cavities resulting in high reversibility. The strategy of creating ORR and OER bifunctional catalysts in a single conductive hybrid component may pave the way to new cathode architectures for metal air batteries.

Vertically aligned two-dimensional graphene-metal hydroxide hybrid arrays for Li-O₂ batteries

Jixin Zhu, [†] *Michael Metzger,* [‡] *Markus Antonietti* [†] *and Tim-Patrick Fellinger** [†]

[†] Max Planck Institute of Colloids and Interfaces, Department of Colloid Chemistry, Research Campus Golm, Am Mühlenberg 1, 14476 Potsdam, Germany, E-mail: Tim.Fellinger@mpikg.mpg.de

[‡] Chair of Technical Electrochemistry, Technische Universität München, Lichtenbergstrasse 4, 85748 Garching, Germany

KEYWORDS: *Carbon nanosheets, metal hydroxide, bifunctional electrocatalysts, lithium-O_2 battery*

ABSTRACT:

Lithium oxygen batteries (LOBs) are a very promising upcoming technology which however still suffers from low lifespan and dramatic capacities fading. Solid discharge products increase the contact resistance and block the electrochemically active electrodes. The resulting high oxidative potentials and formation of Li_2CO_3 due to electrolyte and carbon electrode decomposition at the positive electrode lead to irreversible deactivation of oxygen evolution reaction (OER) and oxygen reduction reaction (ORR) sites. Here we demonstrate a facile strategy for the scalable production of a new electrode structure constituted of vertically aligned carbon nanosheets and metal hydroxide ($M(OH)_x$@CNS) hybrid arrays, integrating both favorable ORR and OER active materials to construct a bifunctional catalysts for LOBs. Excellent lithium-oxygen battery properties with high specific capacity of 5403 mAh g^{-1} and 12123 mAh g^{-1} referenced to the carbon and $M(OH)_x$ weight, respectively, long cyclability and low charge potentials are achieved in the resulting $M(OH)_x$@CNS cathode architecture. The properties are explained by improved O_2/ion transport properties and spatially limited precipitation of Li_2O_2 nanoparticles inside interstitial cavities resulting in high reversibility. The strategy of creating ORR and OER bifunctional catalysts in a single conductive hybrid component may pave the way to new cathode architectures for metal air batteries.

INTRODUCTION:

Lithium air batteries attract great attention owing to their much higher theoretical energy and power densities compared to lithium ion batteries and a potential utilization as energy storage devices in electric vehicles and other mobile operations.[1-5] However, currently the decomposition of carbon cathode materials and organic electrolytes at high oxidative potentials associated with the formation of Li_2CO_3, results in lower capacity, poor reversibility and cyclability in lithium oxygen batteries (LOBs).[3, 6-9] In this regard, noble metals have been proven to be efficient catalysts for LOBs with sufficient stability, however coming with high cost.[10-15] Thus, great efforts have been devoted to explore effective strategies to design alternative electrocatalysts for LOBs with high activity and stability at low costs.[16-21] Within these, a new generation of carbon materials with well-defined structure and functionality are widely exploited and investigated as cathode materials.[1, 6, 21-24] The electrocatalytic activity of carbons towards oxygen reduction reaction (ORR) are mainly related to their chemical composition (e.g. nitrogen doping), but also influenced by local order and electric conductivity, alongside their morphologies.[17, 25] In this regard, structured carbons hold great promise as electrode materials for high-performance energy storage devices because they facilitate electrolyte immersion, Li^+/O_2 diffusion, and the accommodation of electrode volume swing. Conventional carbons typically serve as good ORR catalysts for LOBs, but show less activity/stability for OER.[1, 4, 10, 17, 23] Heteroatom doped "noble" carbons are a promising class of materials in this regard.[26] However, fabrication of advanced carbon hybrid architectures coupled with both high ORR and OER activities in a single catalyst material for LOB are another desirable option. Previous reports indicate that such hybrid structures can show synergistically improved catalytic activity and chemical stability.[27-28] Rational design of such multifunctional hybrid architectures is however challenging. Both, active

OER and ORR sites must be in proximity. As we need so-called three-phase boundaries for ORR in fuel cells (catalyst-electrolyte-gas), an even more complicated "four-phase" boundary due to the additional requirement of the presence of the OER active phase has to be designed. In case of an insulating OER active phase it is additionally crucial that it is well-connected to the conductive phase (e.g. the doped carbons), and that the conducting phase is continuous. Synergistic effects are especially likely to occur on the nanoscale, where electronic changes e.g. from hetero-junctions are relevant. Nanomaterials additionally have the advantage of enhanced surface areas being reflected in large electrode/electrolyte interfaces, i.e. high electrochemically active surface areas.

Direct growth of OER active low-conductance material, e.g. metal oxides/hydroxides on conductive substrates is a way to overcome their intrinsic poor conductivity.[29-32] Vertically aligned two-dimensional (2D) carbon architectures manifest superior chemical stability and good electric conductivity as well as the aforementioned merits of nanostructures.[33-36] As a result, excellent energy storage properties were obtained from vertically aligned 2D carbon nanosheets in utilization as electrode materials for lithium ion batteries and supercapacitors.[35-36] Such mechanically and chemically robust substrates are interesting candidates for an ORR active substrate as they are percolated, rigidly assembled electrodes with high conductivity, transport porosity and high surface areas. On the other side, intense research has recently been conducted to develop metal hydroxides or layered double hydroxides (LDHs) with controlled structures as highly efficient OER catalysts for water splitting.[37-41] In this respect, merging vertically aligned ORR active carbon nanosheets arrays with metal hydroxides is a promising approach to optimize the electrochemical performance for LOBs.

Here, we report a facile strategy for scalable production of vertically aligned hybrid architectures constructed of nitrogen doped carbon nanosheets and $M(OH)_x$ nanosheets or nanoparticles. The resulting porous $M(OH)_x$@CNS hybrid nanostructures possess high conductivity, high surface area translating to high electrolyte/electrode interfaces, connected interstitial cavities allowing efficient ion/O_2 transportation, and strongly bound CNS and $M(OH)_x$ nanoparticles. Furthermore, hydrogen bonding between the hydroxide and the Li_2O_2 discharge product may facilitate the peroxide crystallization vie discharge. As a consequence, the resulting hybrid nanostructures lead to high capacity, good stability and low overpotentials as they are directly utilized as additive-free electrodes for LOBs. To the best of our knowledge, this is the first report on the vertically aligned $M(OH)_x$@CNS hybrid arrays used for LOBs up to now, which opens a new direction for the development of efficient cathode materials for oxygen activation.

RESULTS AND DISCUSSION:

The synthesis of the vertically aligned and nitrogen doped carbon nanosheets (CNS) with metal hydroxide ($M(OH)_x$@CNS) hybrid arrays is done by a solution process and involves three steps as shown in **Figure 1** (for detail see Experimental Section). First, 3.0 g inorganic salt ($ZnCl_2$ and KCl with mass ratio of 2:1) were mixed into 1 mL 1-Ethyl-3-methylimidazolium dicyanamide (Emim- dca), the nitrogen and carbon source[42] and then the obtained slurry was coated onto freshly cleaned nickel foam. Vertically aligned and nitrogen doped carbon nanosheets (CNS) were obtained after thermal treatment of the mixture under inert atmosphere at 900 $^{\circ}$C for 3 hours and the following removal of inorganic salt by diluted aqueous HCl solution and deionized (DI) water washing. Subsequently, vertically aligned $M(OH)_x$ nanosheets or nanoparticles were grown on the CNS nanosheets via a fast electrodeposition process. The $M(OH)_x$@CNS hybrid

arrays were collected and used as cathode catalyst for lithium-O_2 batteries after cleaning and drying. Note that the fabrication of $M(OH)_x$@CNS hybrid nanosheets in such a simple methodology allows even a potential scale-up for production.
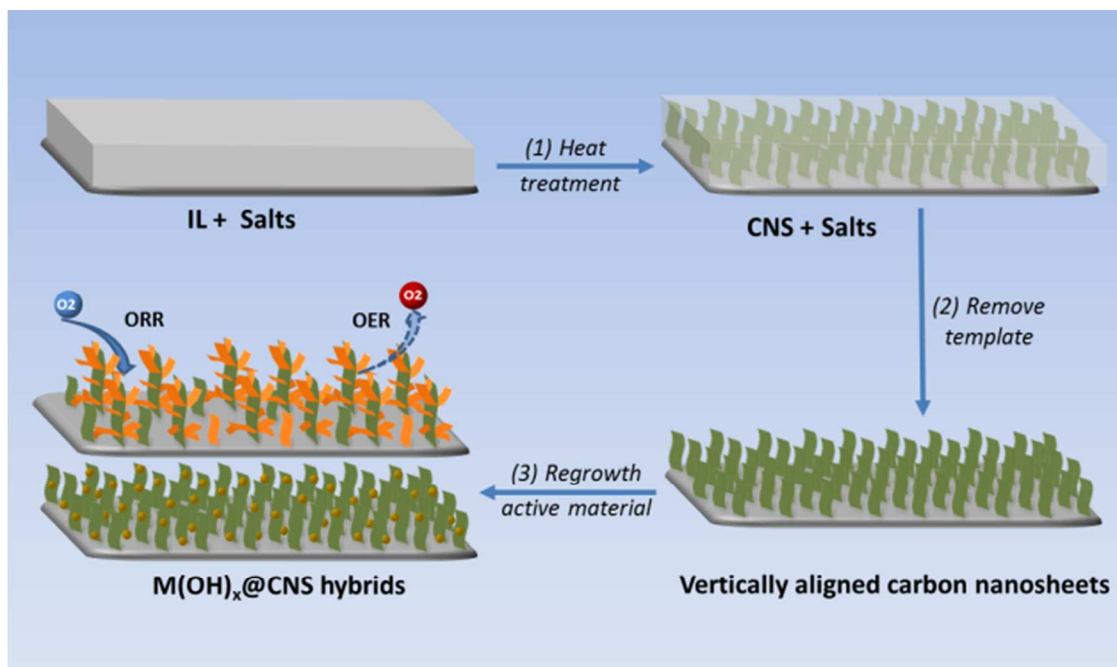

Figure 1. Schematic illustration of the salt-templating process for the formation of vertically aligned two-dimensional (2D) nanosheets and their 2D hybrid nanosheet arrays.

The morphology of the as-prepared products was investigated by field-emission scanning electron microscopy (FE-SEM) as shown in **Figure 2**. After heat treatment at 900 °C for 3 hours and salt removal, a continuous and interconnected film composed of vertically aligned 2D nanosheets, like previously reported, cover the entire surface of the nickel foam. The magnified FE-SEM image in Figure 2b and 2c shows the well-defined primary nanosheets with a thickness of 3 ~ 5 nm and lateral dimension up-to hundreds of nanometers. Such a structure manifests high porosity/surface area, rendering a large electrode/electrolyte interface and allowing for efficient mass transport.
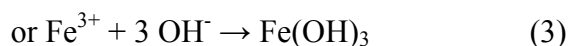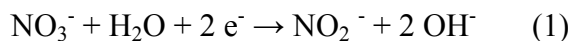
Structure and composition of the as-prepared architectures were further examined by X-ray diffraction (XRD) and Raman spectroscopy (**Figure S1,** Supporting Information). The XRD pattern shows two main reflections located at 44.5 and 52 ^{o} in the as-prepared CNS samples originating from the nickel substrate, whereas the small peak at 26.7 ^{o} is ascribed to graphitic carbon (see Figure S1a and b).[43-44] This observation is further confirmed by Raman spectroscopy as shown in Figure S1c and d. Raman scattering spectroscopy shows three well-resolved peaks located at 1348, 1575, and 2682 cm^{-1} which are characteristic for the D band, G band and 2D band, evidencing the formation of graphitic CNS composed of few-layer graphene.[45-46] In addition, a weak D′ shoulder located at ~1619 cm^{-1} is observed. This is well-known to go along with nitrogen doping, which is crucial to obtain good ORR activity.[47] The content of N in the CNS is around 3.2 % calculated from elemental analysis.
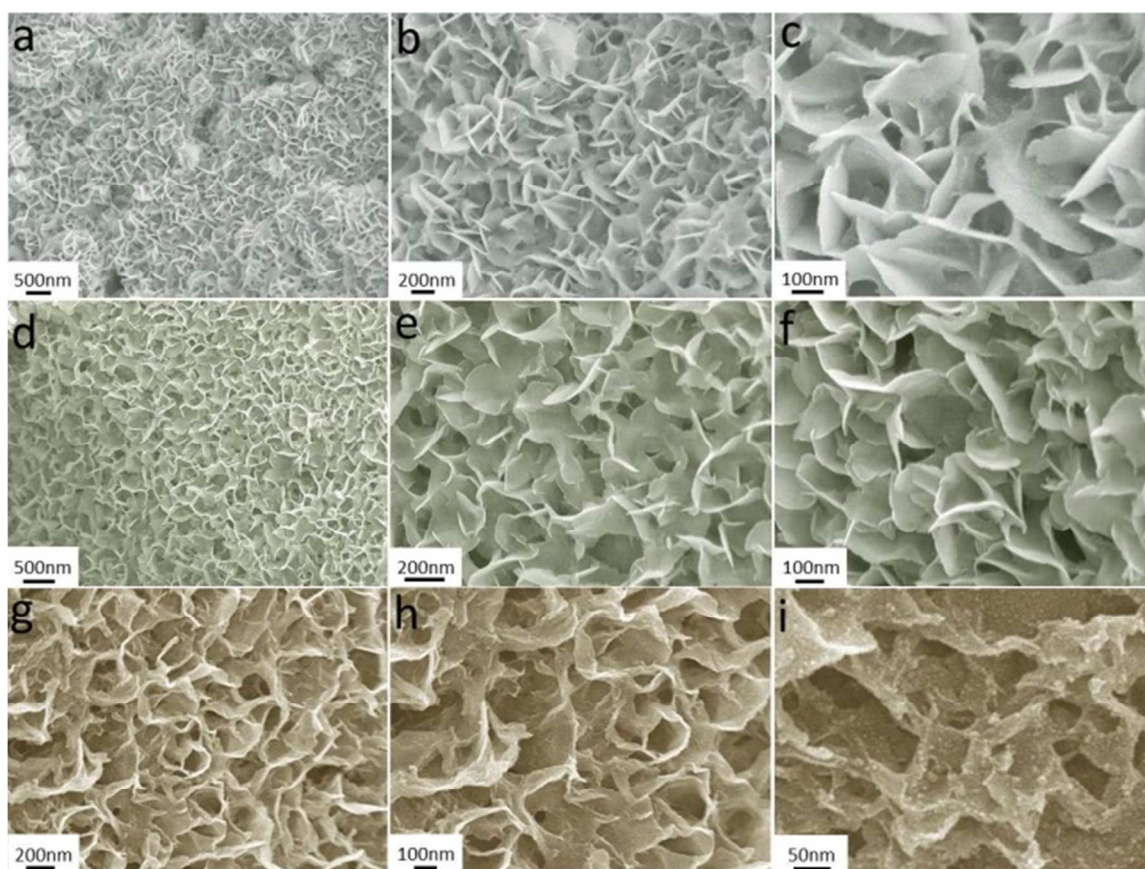
Figure 2. Typical field emission scanning electron microscopy (FESEM) images: (a-c) nitrogen doped graphitic carbon nanosheets (CNS) on nickel foam, (d-f) carbon nanosheets with $Co(OH)_2$ nanosheet hybrids ($Co(OH)_2$@CNS) and (g-i) carbon nanosheets with $Fe(OH)_3$ nanosheet hybrids ($Fe(OH)_3$@CNS).

In order to implement both high catalytic activity of ORR and OER in a single system, very thin $Co(OH)_2$ nanosheets and very small spherical $Fe(OH)_3$ nanoparticles were deposited on the resulting vertically aligned CNS products via fast electrodeposition. Shortly, the hydroxides were directly deposited onto the CNSs arrays from 10 mM aqueous $Co(NO_3)_2 \cdot 6H_2O$ or 10 mM aqueous $Fe(NO_3)_3 \cdot 6\,H_2O$ solution at room temperature. The deposition potential was -1.0 V vs. SCE. The electrodeposition process of the cobalt hydroxide and iron hydroxide can be expressed as follows:[48]

$$NO_3^- + H_2O + 2\,e^- \rightarrow NO_2^{\,-} + 2\,OH^- \qquad (1)$$

$$Co^{2+} + 2\,OH^- \rightarrow Co(OH)_2 \qquad (2)$$

$$\text{or } Fe^{3+} + 3\,OH^- \rightarrow Fe(OH)_3 \qquad (3)$$

The mass m of the metal hydroxide deposit can be calculated according to following equation: $m = 5QM / 8eN_A$, where Q is the deposition charge, M is the relative molecular mass of $Co(OH)_2$ or $Fe(OH)_3$, N_A is the Avogadro constant, and e is the electronic unit charge. The mass loading of the metal hydroxide was calculated by I/t curves, which lead to consistent results with the mass difference calculated by directly weighting the samples before and after the deposition process. Figures 2d-f show that the overall nanosheet structure is retained without apparent change/destruction after $Co(OH)_2$ deposition. The FESEM image demonstrates that the resulting

architecture still comprises of a rough surface and pronounced interstitial cavities. The magnified FESEM image elucidates no structural changes to the former oriented and highly interconnected nanosheets, still showing a thickness of 2 ~ 3 nm and lateral dimension of up to hundreds of nanometers. Interestingly, also the microscopy contrast seems to be unchanged, overall indicating a deposition of small islands in sub-monolayer quantity. Even by increasing the electrodeposition time from 30 to 60 s and even more, there is no obvious change of the general morphology, except for the increasing lateral size of the nanosheets (**Figure S2,** Supporting Information). A cross-sectional view on the coated nickel foam further shows that the nickel foam substrate is fully covered with the vertically aligned nanosheets and that the card house structure of the film gives continuous transport porosity (Figure S2d-e). Beside the $Co(OH)_2$ thin film nanohybrid formation, $Fe(OH)_3$ nanoparticles could easily be deposited on the surface of the CNSs by simply changing the precursor solution from aqueous $Co(NO_3)_2$ solution to aqueous $Fe(NO_3)_2$ solution. As can be observed in Figure 2g-i, the overall morphology of the resulting hybrid architecture is retained, and the magnified FESEM image depicts numerous small nanospheres decorated on the surface of the CNSs. The particle size is ~3 nm with a narrow size distribution (see Figure 2i). After electrodeposition of $Co(OH)_2$ and $Fe(OH)_3$, the wide angle XRD patterns of the two hybrids are unchanged as compared to that of the bare CNS, which show the (002) peak of CNS and Ni peaks without other apparent reflections. These results indicate an amorphous character of the deposited $Co(OH)_2$ and $Fe(OH)_3$. The amorphous character is also obtained in blind experiments, where $Co(OH)_2$ and $Fe(OH)_3$ was electrodeposited directly onto the nickel foam (for more detail see experimental section). SEM imaging reveals that there are numerous nanosheets and nanospheres in the corresponding $Co(OH)_2@Ni$ and $Fe(OH)_3@Ni$ products (**Figure S3**, Supporting Information), while their XRD

patterns also only shows Ni peaks (**Figure S1a**). Raman spectra of the $Co(OH)_2$@CNS and $Fe(OH)_3$@CNS samples show the same aforedescribed characteristic graphitic carbon D band and G band features for the bare CNS, indicating that the overall carbon structure was retained (**Figure S1b**). In the hybrid $Co(OH)_2$@CNS, the peaks located at 463, 508, 602 and 667 cm^{-1} are assigned to $Co(OH)_2$. Reference spectra of $Co(OH)_2$@Ni also possess the same feature and are in line with the literature.[49-51] Likewise, there are two peaks observed at 471 and 681 cm^{-1} for both $Fe(OH)_3$@CNS and $Fe(OH)_3$@Ni, that are therefore assigned to the $Fe(OH)_3$.[52-53] The XPS analysis further reveals the characteristic satellites of Co^{2+} 2p3/2 and 2p1/2 bands located at the binding energies of 780.9, 783.0, 786.2 and 790.0 eV. The signals can be assigned to the $Co(OH)_2$ phase[54-55] within the $Co(OH)_2$@CNS hybrid as shown in **Figure S4 (Supporting Information)**. The characteristic satellites of Fe^{3+} 2p3/2 and 2p1/2 bands at the binding energies of 705.0, 709.0, 712.0, 716.9, 722.0 and 725.0 eV are observed for the $Fe(OH)_3$@CNS hybrid, which confirms the formation of $Fe(OH)_3$ phase.[54] Together these results indicate the formation of amorphous $Co(OH)_2$ and $Fe(OH)_3$ on top of the 2D nanosheet hybrid architectures.

Transmission electron microscopy (TEM) was conducted to further investigate the nanostructure and composition of the obtained hybrid architectures as shown in **Figure 3.** Images of bare CNSs for comparison can be found in **Figure S5** (supporting information).
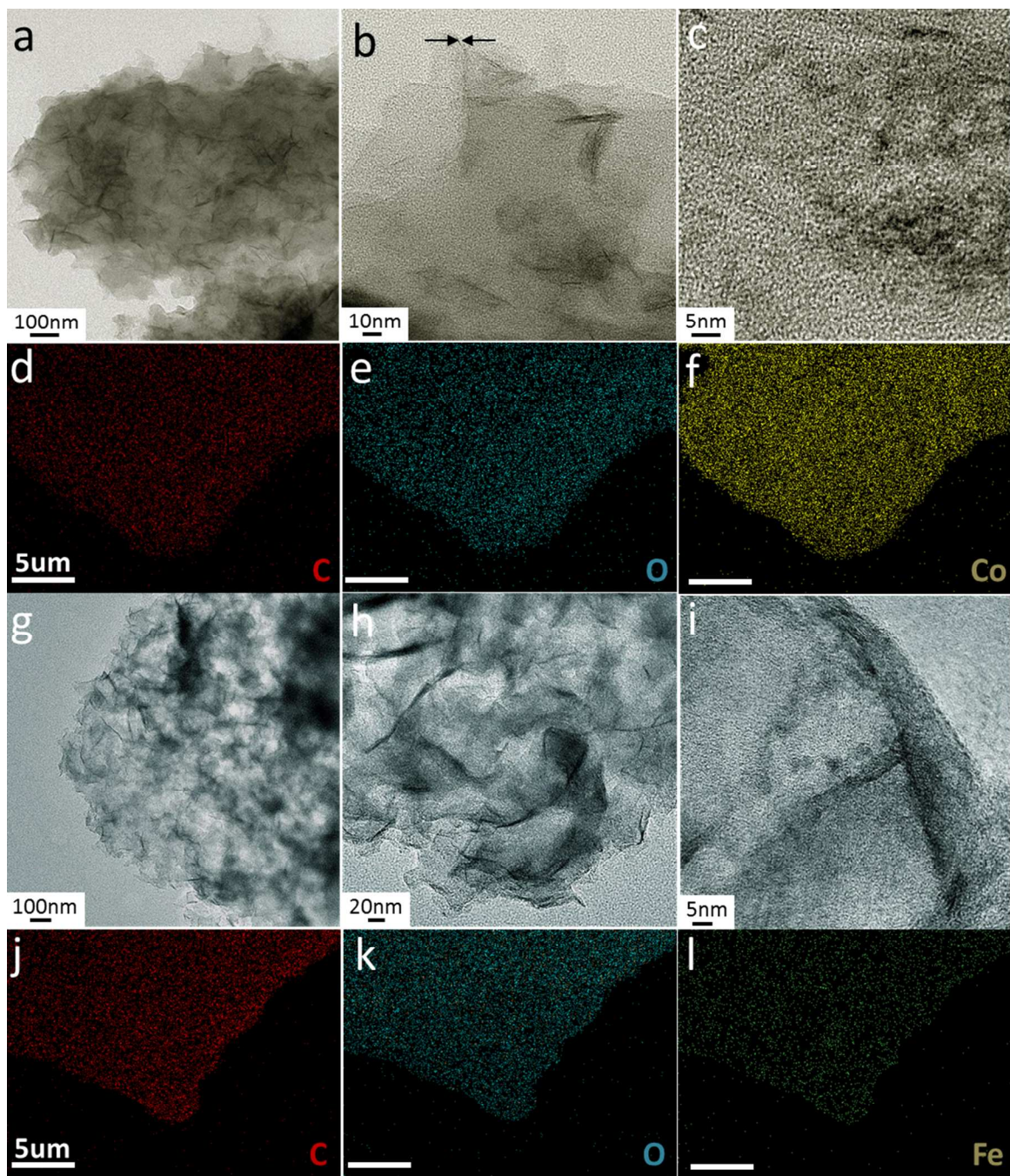
Figure 3. (a-c) Transmission electron microscopy (TEM) images of typical Co(OH)$_2$@CNS hybrid nanosheets, (d-f) elemental mapping of carbon (red), oxygen (blue) and cobalt (yellow), (g-i) TEM images of typical Fe(OH)$_3$@CNS hybrid nanosheets, (i-l) elemental mapping of carbon (red), oxygen (blue) and iron (yellow).

Also by TEM it is clearly observed that the sheets are interconnected, which is crucial for efficient electron transfer. The high-resolution TEM images demonstrate the electron-transparent character of the obviously very thin carbon nanosheets, and confirm the observed nanosheet thickness of around 3-5 nm as well as the composed of graphitic layers (Figure S3b, supporting information). The unique architectural features of $Co(OH)_2$@CNS can further be observed by TEM as shown in Figure 3a-c. The thickness of the hybrid nanosheets is estimated to ~3 nm (an example is marked by arrows in Figure 3b). However, there is no lattice periodicity observed in the $Co(OH)_2$@CNS products owing to the amorphous structure of $Co(OH)_2$ nanosheets (Figure 3c). Furthermore, there is also no obvious phase contrast under the TEM beam among the hybrid because of the very thin thickness and a corresponding good electronic contact. This is confirmed by energy dispersive X-ray (EDX) and elemental mapping analysis, which reveals that the C, O and Co atoms are homogeneously distributed at least on the microscale (Figure 3d-f). The TEM images of $Fe(OH)_3$@CNS suggest the same overall structural feature with respective amorphous $Fe(OH)_3$. The EDX and elemental mapping observations confirm the homogeneous distribution of C, O and Fe atoms in the as-prepared $Fe(OH)_3$@CNS hybrid (Figure 3j-l).

The electrocatalytic activities of bare CNS and $M(OH)_x$@CNS hybrid electrodes towards the electrochemical ORR and OER were studied under aqueous conditions. A typical three-electrode electrochemical cell configuration, using aqueous 0.1 M KOH solution as electrolyte, was employed (**Figure S6**, Supporting Information). It was found that the $Co(OH)_2$@CNS and $Fe(OH)_3$@CNS hybrid electrodes show a strong synergistic effect and indeed exhibit superior ORR/OER properties, that could be used in reversible alkaline electrolyzers/fuel cells. The $Co(OH)_2$@CNS and $Fe(OH)_3$@CNS hybrid electrodes show upshifts of the ORR half-wave

potentials of 144 and 90 mV, respectively, as compared to the bare CNSs. On the other side, very good OER activities are obtained by the nanohybridization with $Co(OH)_2$ and $Fe(OH)_3$. Very small corresponding benchmark overpotentials η_{10} (at 10 mA cm^{-2}) of 270 and 230 mV are obtained for $Co(OH)_2$@CNS and $Fe(OH)_3$@CNS, respectively. Nickel, or more precisely in-situ oxidized nickel is known to catalyze the OER well. The unprocessed foam however has low activity in the ORR and also a comparably higher OER overpotential of 310 mV under the same conditions, showing that the decoration with CNS the respective hybrids is crucial to gain increased activity. In addition to the electrocatalytic activity, the $M(OH)_x$@CNS hybrid architectures reveal desirable structural features of high electrode/electrolyte interface, interstitial mass transport porosity and homogeneously distributed heterojunctions in one system, which renders great promise for utilization as electrode in lithium-oxygen batteries (LOBs) with improved performance. Although, the ORR/OER mechanism in aqueous as compared to non-aqueous conditions is typically different, the observed catalytic activities point to potentially high activity also in non-aqueous electrolyte leading to reduced polarization in LOBs. Therefore in the next step $Co(OH)_2$@CNS and $Fe(OH)_3$@CNS hybrid architectures were systematically studied as electrodes for LOBs as shown in **Figure 4**.
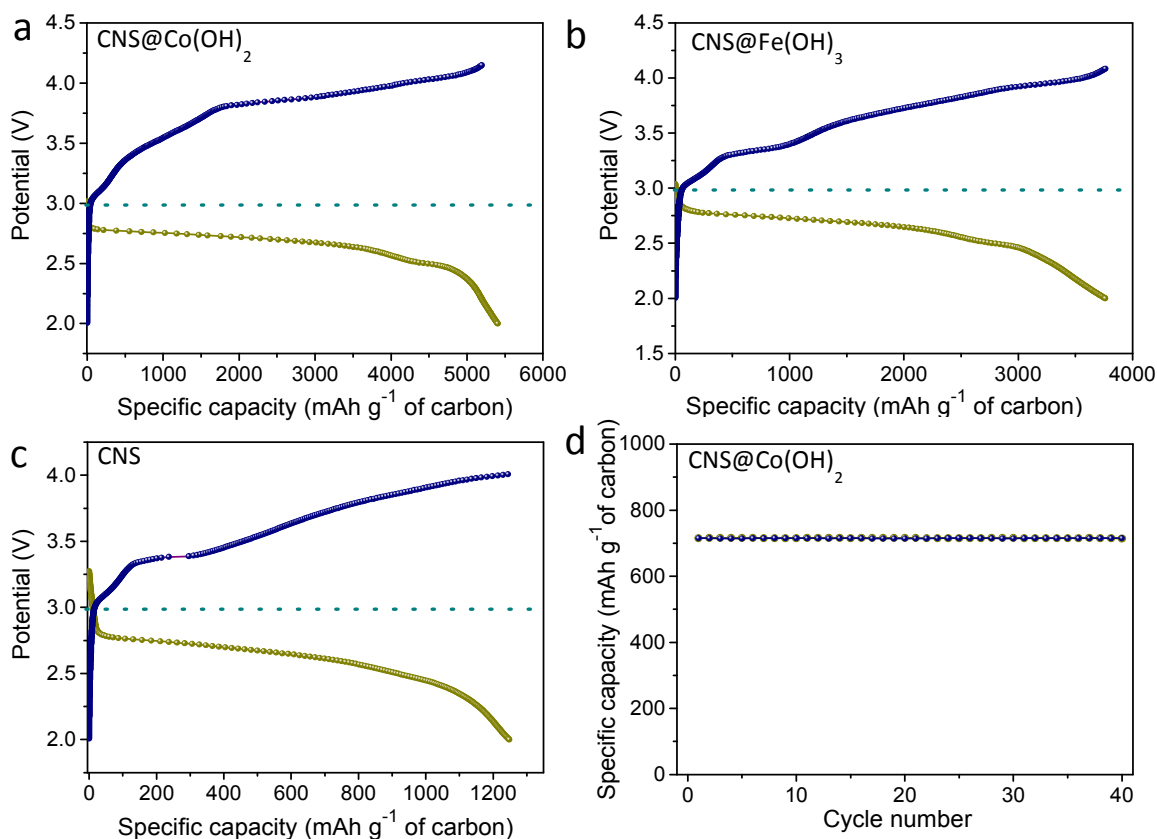
**Figure 4.** (a) Full discharge-charge profile of Co(OH)$_2$@CNS at 75 mA g^{-1}; (b) full discharge-charge profile of Fe(OH)$_3$@CNS at 75 mA g^{-1}; (c) full discharge-charge profile of CNS at 75 mA g^{-1}; (d) Cycle performances of Co(OH)$_2$@CNS under specific capacity limit of 715 mAh g^{-1} in a maximal voltage window between 4.15 and 2.0 V at a current density of 150 mA g^{-1}. Here, all the specific capacities and current densities are calculated based on the mass of carbon.

The pure CNS and M(OH)$_x$@CNS hybrid electrodes were characterized in Li-O$_2$ batteries with Li foil as anode and 0.5 M bis(trifluoromethane)sulfonimide lithium salt (LiCF$_3$SO$_3$) in tetraethylene glycol dimethyl ether (TEGDME) as electrolyte. The full capacities of the pure CNS and M(OH)$_x$@CNS hybrid electrodes were explored by discharging the cell down to 2.0 V at a current density of 75 mA g^{-1}, followed by charging to an equivalent capacity at the same

current density. The pure CNS sample showed a discharge capacity of 1248 mAh g^{-1}. The Co(OH)$_2$@CNS hybrid cathode delivered a high discharge capacity of 5403 mAh g^{-1} (Figure 4a). This value is much higher than that of the pure carbon (1248 mAh g^{-1}) and comparable to the reported values of metal oxide/carbon (5100 mAh g^{-1} for Fe$_2$O$_3$/graphene) and noble metal/carbon (e.g. 5900 mAh g^{-1} for Pd/C) composite electrodes.[1, 12-14, 16, 19, 23] The high discharge capacity was also fully reversible at the potential of 4.15 V, which is considered to be below carbon oxidation potentials.[22] The Fe(OH)$_3$@CNS hybrid also depicts a good capacity of 3762 mAh g^{-1} which can be completely regained at the potential of 4.1 V. Most remarkably, the Co(OH)$_2$@CNS and Fe(OH)$_3$@CNS hybrid architecture allow for a comparably low charge overvoltage of 0.58 and 0.44 V at the specific capacity of 1000 mAh g^{-1}, respectively (**Figure S7**, Supporting Information), which is significantly lower than that of pure CNS (e.g. 0.95 V). Reduced charge overpotentials are expected to reduce side reactions and therefore improve cycling stability. Meanwhile, the corresponding discharge overvoltage decreases from 0.52 V (CNS) to 0.23 V (Co(OH)$_2$@CNS) and 0.19 V (Fe(OH)$_3$@CNS), leading to a higher energy efficiency owing to the improved oxygen reduction reaction (ORR) activity in the hybrid electrodes. The presence of the OER catalyst apparently also reduces the discharge overpotential likely because the hydroxide can facilitate peroxide precipitation/crystallization by means of hydrogen bonding. A strong compatibility of hydroxide and peroxide phases can already be deduced from LiOH impurities in commercial Li$_2$O$_2$, that is prepared from oxidation of LiOH.[56] These excellent LOB properties of M(OH)$_x$@CNS hybrid electrode are ascribed to the integration of efficient ORR activity of CNS and OER activity of M(OH)$_x$ in a single system. As a proof of concept, the pure nickel foam loaded only with Co(OH)$_2$ nanosheets (Figure S3a and b) shows a much lower full discharge capacity of 40 mAh g^{-1} (Figure S7b). The cycling stability

of $Co(OH)_2$@CNS hybrid electrode was also tested with a conventional testing procedure with a current density of 150 mA g^{-1} and a controlled specific capacity of 715 mAh g^{-1} per cycle based on the mass of the CNS to evaluate its further practical applications in LOB as shown in Figure 4d. [12-13, 57-58] A high reversibility of $Co(OH)_2$@CNS is maintained over 40 cycles without capacities loss, which indicates high potential of these new $M(OH)_x$@CNS systems in practical LOB application. The electrochemical results suggest that the reduced charge overpotential leads to good cyclability. The crystallinity of the discharge and charge product samples was further examined by the XRD shown as **Figure S8**. The morphology of the $Co(OH)_2$@CNS samples obtained after discharge and charge process has also been examined by SEM shown in Figure 5. There are three new weak reflections located at 33, 35.3 and 59 o in the discharge product samples originating from the formation of Li_2O_2.[59] These peaks disappeared when the $Li-O_2$ battery was charged back. Due to its superior performance in the LOB cycling experiments, $Co(OH)_2$@CNS was characterized by a combined pressure transducer and On-line Electrochemical Mass Spectrometry (OEMS)[57] approach to further elucidate the governing discharge and charge reactions and the ORR and OER efficiency (**Figure 5**).
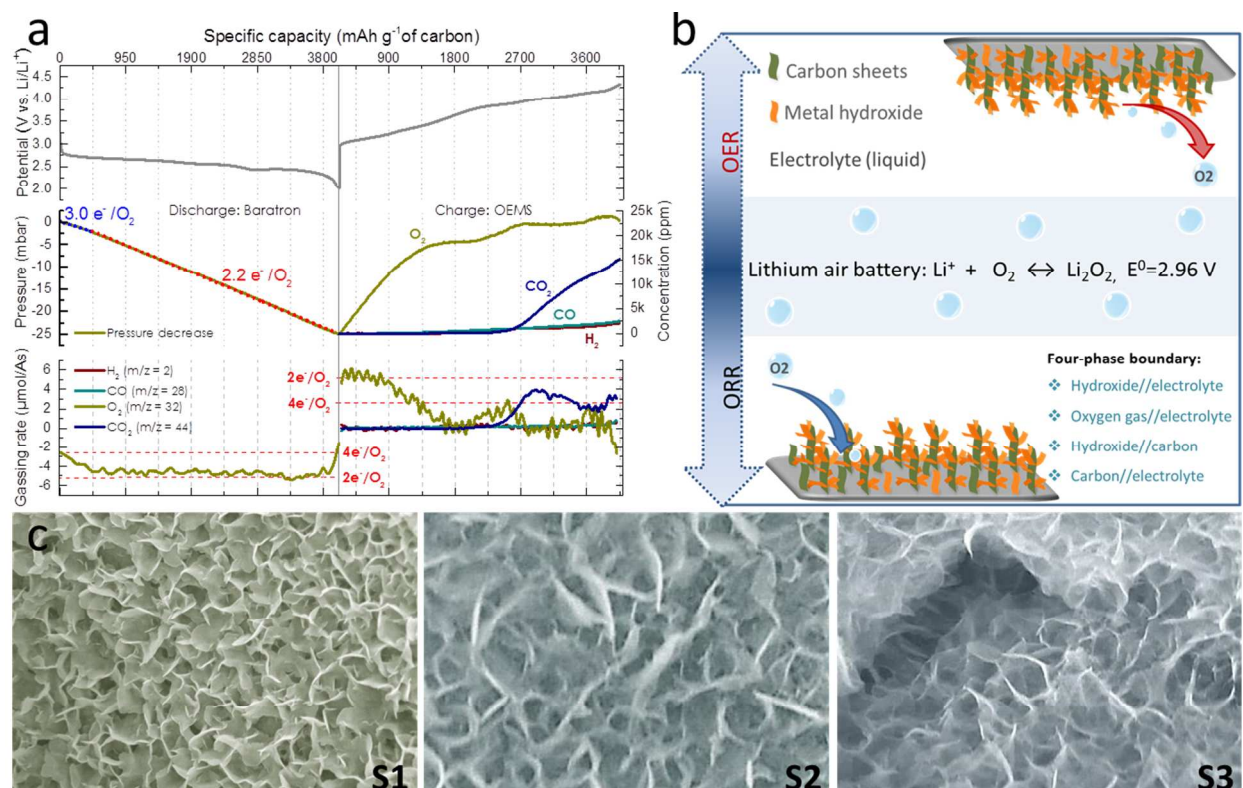
Figure 5. a) Gas analysis of 1st discharge and charge of $Co(OH)_2@CNS$ at 175 mA g^{-1} by combined approach using a Baratron pressure transducer to investigate gas consumption during discharge and OEMS to analyze gas evolution during charge. Upper panel shows potential profile, middle panel absolute gas consumption/evolution, and lower panel gas consumption/evolution rate. Dashed lines indicate respective values for $2e^-/O_2$ and $4 e^-/O_2$. b) Schematic illustration the mechanism of $Co(OH)_2@CNS$ electrode for lithium oxygen battery with four-phase boundary. c) SEM image of the $Co(OH)_2@CNS$ before Li-O_2 test (S1), SEM image of the $Co(OH)_2@CNS$ after discharge (S2), SEM image of the $Co(OH)_2@CNS$ after charge back (S3).

The observed capacities (upper panel in Figure 5) at galvanostatic cycling at 3990 mA g^{-1} at a current density of 175 mA g^{-1} (based on the mass of carbon), and the obtained voltage profiles are in good agreement with the LOB experiment described above, proving that $Co(OH)_2@CNS$

has an identical electrochemical performance in the in-situ cell design. The gas consumption during discharge in pure O_2 is monitored with a Baratron pressure transducer, revealing a total consumption of 25 mbar ($\approx$23 µmol of O_2) and two characteristic regimes: during the initial 470 mAh g-1 of the discharge O_2 is consumed at a rate equivalent to 3.0 e$^-$/O_2 indicating a superposition of a 2 and a 4 e$^-$/O_2 process. The main fraction of the discharge is, however, at 2.2 e$^-$/O_2, implying that Li_2O_2 is the main discharge product formed on Co(OH)$_2$@CNS. It is to mention that in aqueous media it was previously observed that ionic liquid derived carbon can show high selectivity to either a 2 or a 4 electron process depending on the carbon composition.[60-61] The gas evolution during charging reveals that initially O_2 is the only gaseous reaction product, and the gas evolution rate is consistent with a 2e$^-$/O_2 process, indicating that Li_2O_2 formed during discharge is electro-oxidized at the Co(OH)$_2$@CNS surface. Remarkably, most of the O_2 release happens at potentials below 3.9 V, which is consistent with the superior OER activity of Co(OH)$_2$@CNS reported in Figure S6. In the second half of charge (specific capacity > 2496 mAh g^{-1}) at potentials above 3.9 V however considerable amounts of CO_2 and small amounts of CO are released, most probably as a result of electrolyte oxidation. The 1st cycle ORR/OER efficiency can be calculated by dividing the O_2 concentration at the end of charge (23000 ppm $\approx$ 9 µmol) by the moles of O_2 consumed during discharge, resulting in an ORR to OER ratio of 40%. Apparently, a considerable fraction of the oxygen is consumed by side reactions (like formation of Li_2CO_3) already at these voltages. It is also possible that the desired discharge product (Li_2O_2/Li_2O) cannot entirely enter the charge cycle. Consequently, a considerably fraction of the oxygen is trapped and the constant charging current is instead sustained by electrolyte oxidation releasing CO/CO_2. All in all, the gas analysis shows that a good reversibility could be obtained by restricting the operation to shallow cycling with a

capacity limit < 2496 mAh g^{-1}. Unless the charge overvoltage is low and the electrochemical measurements indicate full reversibility, the gas analysis reveals side reactions above 3.9 V vs Li/Li+ and underlines the complexity of Li-oxygen batteries. Figure 5b illustrates the speculated discharge/charge reactions occurring in the proposed Li-oxygen battery. The presented architecture of M(OH)x@CNS hybrid nanosheet thereby integrated favourable ORR/OER activity in a single electrode with multi-level cavities, which are crucial for improving the transportation of O_2 including absorption and desorption as well as limiting the growth of discharged Li_2O_2 products to the nanosize. The morphology of the $Co(OH)_2$@CNS samples obtained after discharge and charge process has been examined by SEM and XRD shown as Figure 5c. After discharge process, there are many fine nanocrystals covering the surface of $Co(OH)_2$@CNS nanosheets, which is similar to a previous report[14] and again speaks for the ease of peroxide precipitation/crystallization mediated by hydrogen bonding to the hydroxide phase.

CONCLUSION:

Here, we reported a facile strategy for scalable production of vertically aligned hybrid nanosheets on nickel foam and the utilization as electrodes for lithium-oxygen batteries. The resulting architectures are composed of very thin metal hydroxides and nitrogen doped graphitic carbon nanosheets as combined functional building blocks that integrate active OER and ORR components in a single system to form a bifunctional catalysts. The strong mechanical connection of the hybrids to the nickel substrate prevents the use of binders and mediates good electric contact. The nanoporous card-house type of structure can confine the growth of Li_2O_2 throughout the battery charging and improve transportation of O_2. Therefore, enhanced oxygen activation properties as well as high specific capacities (5403 mAh g^{-1} at 4.15 V for the Co(OH) hybrid), low charge potentials and excellent reversibility are observed. Despite the reversibility,
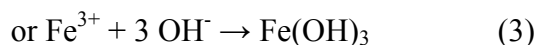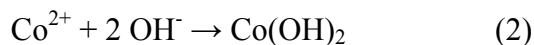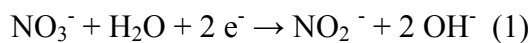
detailed gas analysis reveals side reactions contributing at potentials already below 4.15 V, i.e. before carbon oxidation is expected. Stable cycling was possible with a voltage cut-off of 3.9 V at a capacity of 2496 mAh g^{-1}. This is the first report on metal hydroxides and carbon hybrids for LOB, which opens an optional path to create ORR and OER bifunctional components as a single catalyst with advantageous pore structure as new cathodes for the Li-O$_2$ cell. The presented electrode architecture is promising for LOB application considering ongoing progress in the development of suitable electrolytes.

EXPERIMENTAL SECTION:

Fabrication of vertically aligned N-doped graphitic carbon nanosheets (CNS): In a typical process, 1mL 1-Ethyl-3-methylimidazolium dicyanamide (Emim-dca) are mixed with a salt mixture of ZnCl$_2$/KCl (2g/1g) by grinding. Subsequently, the slurry was coated on the as cleaned nickel foam substrate, followed by heat treatment at 900 ^{o}C for 3 hours under N$_2$ atmosphere. Here, the nickel foam is washed by diluted HCl aqueous solution (0.5 M), deionized water, and ethanol and finally dried in vacuum oven. Finally, the products are collected after washing with 0.5 M aqueous HCl, deionized water and absolute ethanol.

Fabrication of vertically aligned N-doped graphitic carbon/metal hydroxide hybrid nanosheets (M(OH)$_x$@CNS): Cobalt hydroxide nanosheet arrays and iron hydroxide nanoparticles on CNS were directly deposited from 10 mM Co(NO$_3$)$_2$·$_6$H$_2$O or 10 mM Fe(NO$_3$)$_3$·$_6$H$_2$O solution at room temperature using a electrochemical workstation (Gamry Instruments, Inc.). The deposition potential was -1.0 V vs. SCE. The corresponding electrodes are as following: the CNS on nickel foam as working electrode, Ag/AgCl as the reference electrode and nickel coil as counter

electrode. The electrodeposition process of the cobalt hydroxide and iron hydroxide can be expressed as follows:[48]

$$NO_3^- + H_2O + 2\ e^- \rightarrow NO_2^{\ -} + 2\ OH^- \quad (1)$$

$$Co^{2+} + 2\ OH^- \rightarrow Co(OH)_2 \quad\quad (2)$$

$$\text{or } Fe^{3+} + 3\ OH^- \rightarrow Fe(OH)_3 \quad\quad (3)$$

The weight of the deposite (m) can be calculated according to following equation: $m = 5QM / 8eN_A$, Q is the deposition charge, M is the relative molecular mass of $Co(OH)_2$ or $Fe(OH)_3$, N_A is the Avogadro number, and e is the electronic charge.

Electrodeposition of metal hydroxides on nickel form: Cobalt hydroxide nanosheet arrays and iron hydroxide nanoparticles on Nickel foam were directly deposited from 10 mM $Co(NO_3)_2 \cdot 6H_2O$ or 10 mM $Fe(NO_3)_3 \cdot 6H_2O$ solution at room temperature using a electrochemical workstation (Gamry Instruments, Inc.). The deposition potential was -1.0 V vs. SCE. The corresponding electrodes are as following: nickel foam as working electrode, Ag/AgCl as the reference electrode and nickel coil as counter electrode. The electrodeposition process of the cobalt hydroxide and iron hydroxide can be expressed as follows:

Electrocatalytic activity for oxygen reduction reaction and oxygen evolution reaction testing: The electrocatalytic properties were tested in a conventional three-electrode cell using a Reference 600 potentiostat/galvanostat equipped with a RDE 710 Rotating Electrode setup (Gamry Instruments, Inc.). The samples on the nickel foam were directly assembled into a stainless steel electrode (Gamry Lithium battery standard cell kit) as working electrode and the measurements were conducted in O_2-staturated 0.1 M KOH using Ag/AgCl with saturated KCl

solution as reference electrode and Pt wire as counter electrode. Linear sweep voltammetry was carried out at 1 mV s^{-1} for the polarization curves. All polarization curves were iR corrected after preliminary measurement of R_u.

Lithium oxygen battery properties measurements: The as-prepared samples on nickel foam were directly used as additive and binder-free electrodes and were assembled in an Ar-filled glovebox with concentrations of moisture and oxygen below 1.0 ppm. Electrochemical measurements were carried out on the designed Li-O$_2$ cells with lithium metal as the counter/reference electrode, microfiber filter membrane (Whatman GF/D) as the separator, and electrolyte solution obtained by dissolving 0.5 M LiCF$_3$SO$_3$ into tetra(ethylene) glycol dimethyl ether (TEGDME) as the electrolyte. The charge/discharge voltage profiles were tested with cutoff voltages of 2.0 V for discharging and 4.15 V for charging at a current density of 75 mA g^{-1} (referred to the carbon mass) by using a Gamry reference 3000 potentiostat for all samples. The stabilities are tested at a current density of 150 mA g^{-1} with a controlled specific capacity of 715 mAh g^{-1} per cycle based on the mass of the CNS. Capacities were normalized to the carbon mass.

Gas analysis measurements: In-situ gas analysis was performed for Co(OH)$_2$@CNS cathodes assembled in custom cell hardware[62-63] using Li foil anodes, two glass fiber separator sheets and 400 µl 0.5 M bis(trifluoromethane)sulfonimide lithium salt (LiCF$_3$SO$_3$) in tetraethylene glycol dimethyl ether (TEGDME) as electrolyte. For gas analysis during discharge, a Baratron pressure transducer (Baratron 627D, MKS Instruments)[64] was coupled to the On-line Electrochemical Mass Spectrometry (OEMS) cell setup which was previously described in detail.[62] The cell was galvanostatically discharged to 2.0 V after 2 h rest at open circuit voltage (OCV) at 3990 mA g^{-1} at a current density of 175 mA g^{-1} (based on the mass of carbon) in pure O$_2$ and the oxygen consumption was monitored as pressure decrease in the cell. The gas evolution during charge

was measured after the cell was purged with Ar and held at OCV for 2 hours after discharge. It was galvanostatically charged at 4010 mA g^{-1} to a potential of 4.3 V. Conversion of the mass spectrometer currents to concentrations was done for oxygen, carbon dioxide, and carbon monoxide and hydrogen using a calibration gas (H_2, O_2, CO, and CO_2 at 2000 ppm each in argon).

Characterizations: The morphologies of the samples were investigated by using a field-emission scanning electron microscopy (FESEM, JEOL 5600). The samples deposited on nickel foam were immersed in ethanol and collected after sonication to drop-cast onto a holey amorphous carbon film on a copper grid. The TEM, EELS and EDS measurements of the samples were characterized by using a transmission electron microscope (TEM, JEOL 2100F) operating at an acceleration voltage of 200 kV. XRD measurements were performed on a D8 Diffractometer from Bruker instruments (Cu K α radiation, $\lambda = 0.154$ nm) equipped with a scintillation counter. The micro-Raman spectroscopy (Renishaw inVia Raman Spectroscope) experiments were carried out under ambient conditions by using a green laser (532 nm) as the light source.

ASSOCIATED CONTENT :

Supporting Information. PXRD, Raman, FESEM and cross-section FESEM, XPS, TEM, linear sweep voltammetry and charge-discharge results of the hybrid materials and/or reference samples are supplied as Supporting Information. This material is available free of charge via the Internet at http://pubs.acs.org."

AUTHOR INFORMATION:

Corresponding Author

* Dr. T.-P. Fellinger, Max Planck Institute of Colloids and Interfaces, Department of Colloid Chemistry, Research Campus Golm, Am Mühlenberg 1, 14476 Potsdam, Germany

E-mail: Tim.Fellinger@mpikg.mpg.de

ACKNOWLEDGEMENT

REFERENCES

1. Ogasawara, T.; Débart, A.; Holzapfel, M.; Novák, P.; Bruce, P. G., Rechargeable Li_2O_2 Electrode for Lithium Batteries. *J. Am. Chem. Soc.* **2006,** *128*, 1390-1393.

2. Abraham, K. M.; Jiang, Z., A Polymer Electrolyte-based Rechargeable Lithium/Oxygen Battery. *J. Electrochem. Soc.* **1996,** *143*, 1-5.

3. Girishkumar, G.; McCloskey, B.; Luntz, A. C.; Swanson, S.; Wilcke, W., Lithium−Air Battery: Promise and Challenges. *J. Phys. Chem. Lett.* **2010,** *1*, 2193-2203.

4. Lu, Y.-C.; Gasteiger, H. A.; Parent, M. C.; Chiloyan, V.; Shao-Horn, Y., The Influence of Catalysts on Discharge and Charge Voltages of Rechargeable Li–Oxygen Batteries. *Electrochem. Solid St.* **2010,** *13*, A69.

5. Scrosati, B.; Hassoun, J.; Sun, Y.-K., Lithium-ion Batteries. A Look into the Future. *Energ. Environ. Sci.* **2011,** *4*, 3287-3295.

6. Lee, J. S.; Kim, S. T.; Cao, R.; Choi, N. S.; Liu, M.; Lee, K. T.; Cho, J., Metal-Air Batteries with High Energy Density: Li-Air versus Zn-Air. *Adv. Energy Mater.* **2011,** *1*, 34-50.

7. McCloskey, B. D.; Bethune, D. S.; Shelby, R. M.; Girishkumar, G.; Luntz, A. C., Solvents' Critical Role in Nonaqueous Lithium–Oxygen Battery Electrochemistry. *J. Phys. Chem. Lett.* **2011,** *2*, 1161-1166.

8. Meini, S.; Piana, M.; Beyer, H.; Schwammlein, J.; Gasteiger, H. A., Effect of Carbon Surface Area on First Discharge Capacity of Li-O_2 Cathodes and Cycle-Life Behavior in Ether-Based Electrolytes. *J. Electrochem. Soc.* **2012,** *159*, A2135-A2142.

9. Grande, L.; Paillard, E.; Hassoun, J.; Park, J.-B.; Lee, Y.-J.; Sun, Y.-K.; Passerini, S.; Scrosati, B., The Lithium/Air Battery: Still an Emerging System or a Practical Reality? *Adv. Mater.* **2015**, *27*, 784-800.

10. Lu, Y. C.; Gasteiger, H. A.; Shao-Horn, Y., Catalytic Activity Trends of Oxygen Reduction Reaction for Nonaqueous Li-Air Batteries. *J. Am. Chem. Soc.* **2011,** *133*, 19048-19051.

11. Huang, X.; Yu, H.; Tan, H.; Zhu, J.; Zhang, W.; Wang, C.; Zhang, J.; Wang, Y.; Lv, Y.; Zeng, Z.; Liu, D.; Ding, J.; Zhang, Q.; Srinivasan, M.; Ajayan, P. M.; Hng, H. H.; Yan, Q., Carbon Nanotube-Encapsulated Noble Metal Nanoparticle Hybrid as a Cathode Material for Li-Oxygen Batteries. *Adv. Funct. Mater.* **2014,** *24*, 6516-6523.

12. Peng, Z.; Freunberger, S. A.; Chen, Y.; Bruce, P. G., A Reversible and Higher-Rate Li-O2 Battery. *Science* **2012,** *337*, 563-566.

13. Ottakam Thotiyl, M. M.; Freunberger, S. A.; Peng, Z.; Chen, Y.; Liu, Z.; Bruce, P. G., A Stable Cathode for the Aprotic Li-O_2 Battery. *Nat. Mater.* **2013,** *12*, 1050-1056.

14. Xu, J. J.; Wang, Z. L.; Xu, D.; Zhang, L. L.; Zhang, X. B., Tailoring Deposition and Morphology of Discharge Products towards High-Rate and Long-Life Lithium-Oxygen Batteries. *Nat. Commun.* **2013,** *4*, 2438.

15. Zhang, C.; Tang, D.; Hu, X.; Liu, X.; Zhang, T.; Zhou, H., Scalable Synthesis and Excellent Catalytic Effect of Hydrangea-like RuO_2 Mesoporous Materials for Lithium–O_2 Batteries. *Energy Storage Mater.* **2016,** *2*, 8-13.

16. Oh, S. H.; Black, R.; Pomerantseva, E.; Lee, J. H.; Nazar, L. F., Synthesis of a Metallic Mesoporous Pyrochlore as a Catalyst for Lithium-O_2 Batteries. *Nat. Chem.* **2012,** *4*, 1004-1010.

17. Cao, R.; Lee, J. S.; Liu, M. L.; Cho, J., Recent Progress in Non-Precious Catalysts for Metal-Air Batteries. *Adv. Energy Mater.* **2012,** *2*, 816-829.

18. Shao, Y.; Park, S.; Xiao, J.; Zhang, J.-G.; Wang, Y.; Liu, J., Electrocatalysts for Nonaqueous Lithium–Air Batteries: Status, Challenges, and Perspective. *ACS Catal.* **2012,** *2*, 844-857.

19. Ryu, W. H.; Yoon, T. H.; Song, S. H.; Jeon, S.; Park, Y. J.; Kim, I. D., Bifunctional Composite Catalysts Using Co_3O_4 Nanofibers Immobilized on Nonoxidized Graphene Nanoflakes for High-Capacity and Long-Cycle $Li-O_2$ Batteries. *Nano Lett.* **2013,** *13*, 4190-4197.

20. Xu, J. J.; Xu, D.; Wang, Z. L.; Wang, H. G.; Zhang, L. L.; Zhang, X. B., Synthesis of Perovskite-based Porous $La_{0.75}Sr_{0.25}MnO_3$ Nanotubes as a Highly Efficient Electrocatalyst for Rechargeable Lithium-Oxygen Batteries. *Angew. Chem. Int. Ed.* **2013,** *52*, 3887-3890.

21. Zhang, T.; Zhou, H., A Reversible Long-Life Lithium-Air Battery in Ambient Air. *Nat. Commun.* **2013,** *4*, 1817.

22. Shui, J.; Du, F.; Xue, C.; Li, Q.; Dai, L., Vertically Aligned N-Doped Coral-like Carbon Fiber Arrays as Efficient Air Electrodes for High-Performance Nonaqueous $Li-O_2$ Batteries. *ACS nano* **2014,** *8*, 3015-3022.

23. Zhang, G. Q.; Zheng, J. P.; Liang, R.; Zhang, C.; Wang, B.; Hendrickson, M.; Plichta, E. J., Lithium–Air Batteries Using SWNT/CNF Buckypapers as Air Electrodes. *J. Electrochem. Soc.* **2010,** *157*, A953.

24. Luntz, A. C.; McCloskey, B. D., Nonaqueous Li-Air Batteries: a Status Report. *Chem. Rev.* **2014,** *114*, 11721117-11721150.

25. Zhu, J.; Zhu, T.; Zhou, X.; Zhang, Y.; Lou, X. W.; Chen, X.; Zhang, H.; Hng, H. H.; Yan, Q., Facile Synthesis of Metal Oxide/Reduced Graphene Oxide Hybrids with High Lithium Storage Capacity and Stable Cyclability. *Nanoscale* **2011,** *3*, 1084-1089.

26. Sakaushi, K.; Fellinger, T.-P.; Antonietti, M., Bifunctional Metal-Free Catalysis of Mesoporous Noble Carbons for Oxygen Reduction and Evolution Reactions. *ChemSusChem* **2015,** *8*, 1156-1160.

27. Ren, J.; Antonietti, M.; Fellinger, T.-P., Efficient Water Splitting Using a Simple Ni/N/C Paper Electrocatalyst. *Adv. Energy Mater.* **2015,** *5*, 1401660.

28. Zhang, C.; Antonietti, M.; Fellinger, T.-P., Blood Ties: Co_3O_4 Decorated Blood Derived Carbon as a Superior Bifunctional Electrocatalyst. *Adv. Funct. Mater.* **2014,** *24*, 7655-7665.

29. Fan, G.; Li, F.; Evans, D. G.; Duan, X., Catalytic Applications of Layered Double Hydroxides: Recent Advances and Perspectives. *Chem. Soc. Rev.* **2014,** *43*, 7040-7066.

30. Liu, J.; Li, Y.; Huang, X.; Li, G.; Li, Z., Layered Double Hydroxide Nano- and Microstructures Grown Directly on Metal Substrates and Their Calcined Products for Application as Li-Ion Battery Electrodes. *Adv. Funct. Mater.* **2008,** *18*, 1448-1458.

31. Zhou, W.; Zhu, J.; Cheng, C.; Liu, J.; Yang, H.; Cong, C.; Guan, C.; Jia, X.; Fan, H. J.; Yan, Q.; Li, C. M.; Yu, T., A General Strategy toward Graphene@Metal Oxide Core–Shell Nanostructures for High-Performance Lithium Storage. *Energ. Environ. Sci.* **2011,** *4*, 4954-4961.

32. Yuan, C.; Li, J.; Hou, L.; Zhang, X.; Shen, L.; Lou, X. W. D., Ultrathin Mesoporous $NiCo_2O_4$ Nanosheets Supported on Ni Foam as Advanced Electrodes for Supercapacitors. *Adv. Funct. Mater.* **2012,** *22*, 4592-4597.

33. Wu, Y.; Qiao, P.; Chong, T.; Shen, Z., Carbon Nanowalls Grown by Microwave Plasma Enhanced Chemical Vapor Deposition. *Adv. Mater.* **2002,** *14*, 64-67.

34. Malesevic, A.; Kemps, R.; Vanhulsel, A.; Chowdhury, M. P.; Volodin, A.; Van Haesendonck, C., Field Emission from Vertically Aligned Few-layer Graphene. *J. Appl. Phys.* **2008,** *104*, 084301.

35. Xiao, X.; Liu, P.; Wang, J. S.; Verbrugge, M. W.; Balogh, M. P., Vertically Aligned Graphene Electrode for Lithium Ion Battery with High Rate Capability. *Electrochem. Commun.* **2011,** *13*, 209-212.

36. Bo, Z.; Zhu, W.; Ma, W.; Wen, Z.; Shuai, X.; Chen, J.; Yan, J.; Wang, Z.; Cen, K.; Feng, X., Vertically Oriented Graphene Bridging Active-Layer/Current-Collector Interface for Ultrahigh Rate Supercapacitors. *Adv. Mater.* **2013,** *25*, 5799-5806.

37. Subbaraman, R.; Tripkovic, D.; Chang, K. C.; Strmcnik, D.; Paulikas, A. P.; Hirunsit, P.; Chan, M.; Greeley, J.; Stamenkovic, V.; Markovic, N. M., Trends in Activity for the Water Electrolyser Reactions on 3d M(Ni,Co,Fe,Mn) Hydr(oxy)oxide Catalysts. *Nat. Mater.* **2012,** *11*, 550-557.

38. Chen, S.; Duan, J.; Jaroniec, M.; Qiao, S. Z., Three-dimensional N-doped Graphene Hydrogel/NiCo Double Hydroxide Electrocatalysts for Highly Efficient Oxygen Evolution. *Angew. Chem.* **2013,** *52*, 13567-13570.

39. Gong, M.; Li, Y.; Wang, H.; Liang, Y.; Wu, J. Z.; Zhou, J.; Wang, J.; Regier, T.; Wei, F.; Dai, H., An Advanced Ni-Fe Layered Double Hydroxide Electrocatalyst for Water Oxidation. *J. Am. Chem. Soc.* **2013,** *135*, 8452-8455.

40. Gao, M.; Sheng, W.; Zhuang, Z.; Fang, Q.; Gu, S.; Jiang, J.; Yan, Y., Efficient Water Oxidation using Nanostructured Alpha-Nickel-Hydroxide as an Electrocatalyst. *J. Am. Chem. Soc.* **2014,** *136* (19), 7077-7084.

41. Song, F.; Hu, X., Exfoliation of Layered Double Hydroxides for Enhanced Oxygen Evolution Catalysis. *Nat. Commun.* **2014,** *5*, 4477.

42. Zhu, J.; Sakaushi, K.; Clavel, G.; Shalom, M.; Antonietti, M.; Fellinger, T.-P., A General Salt-Templating Method To Fabricate Vertically Aligned Graphitic Carbon Nanosheets and Their Metal Carbide Hybrids for Superior Lithium Ion Batteries and Water Splitting. *J. Am. Chem. Soc.* **2015,** *137*, 5480-5485.

43. Hu, H.; Zhao, Z.; Wan, W.; Gogotsi, Y.; Qiu, J., Ultralight and Highly Compressible Graphene Aerogels. *Adv. Mater.* **2013,** *25*, 2219-2223.

44. Yang, X.; Zhu, J.; Qiu, L.; Li, D., Bioinspired Effective Prevention of Restacking in Multilayered Graphene Films: Towards the Next Generation of High-Performance Supercapacitors. *Adv. Mater.* **2011,** *23*, 2833-2838.

45. Chen, Z.; Ren, W.; Gao, L.; Liu, B.; Pei, S.; Cheng, H.-M., Three-Dimensional Flexible and Conductive Interconnected Graphene Networks Grown by Chemical Vapour Deposition. *Nat. Mater.* **2011,** *10*, 424-428.

46. Huang, X.; Yin, Z.; Wu, S.; Qi, X.; He, Q.; Zhang, Q.; Yan, Q.; Boey, F.; Zhang, H., Graphene-Based Materials: Synthesis, Characterization, Properties, and Applications. *Small* **2011,** *7*, 1876-1902.

47. Ci, L.; Song, L.; Jin, C.; Jariwala, D.; Wu, D.; Li, Y.; Srivastava, A.; Wang, Z. F.; Storr, K.; Balicas, L.; Liu, F.; Ajayan, P. M., Atomic Layers of Hybridized Boron Nitride and Graphene Domains. *Nat. Mater.* **2010,** *9*, 430-435.

48. Hercule, K. M.; Wei, Q.; Khan, A. M.; Zhao, Y.; Tian, X.; Mai, L., Synergistic Effect of Hierarchical Nanostructured $MoO_2/Co(OH)_2$ with Largely Enhanced Pseudocapacitor Cyclability. *Nano Lett.* **2013,** *13*, 5685-5691.

49. Pauporté, T.; Mendoza, L.; Cassir, M.; Bernard, M. C.; Chivot, J., Direct Low-Temperature Deposition of Crystallized CoOOH Films by Potentiostatic Electrolysis. *J. Electrochem. Soc.* **2005,** *152*, C49.

50. Lee, K. K.; Loh, P. Y.; Sow, C. H.; Chin, W. S., CoOOH Nanosheet Electrodes: Simple Fabrication for Sensitive Electrochemical Sensing of Hydrogen Peroxide and Hydrazine. *Biosens. Bioelectron.* **2013,** *39*, 255-260.

51. Liu, Y.-C.; Koza, J. A.; Switzer, J. A., Conversion of Electrodeposited $Co(OH)_2$ to CoOOH and Co3O4, and Comparison of Their Catalytic Activity for the Oxygen Evolution Reaction. *Electrochim Acta* **2014,** *140*, 359-365.

52. de Faria, D. L. A.; Venâncio Silva, S.; de Oliveira, M. T., Raman Microspectroscopy of Some Iron Oxides and Oxyhydroxides. *J. Raman Spectrosc.* **1997,** *28*, 873-878.

53. Neff, D.; Bellot-Gurlet, L.; Dillmann, P.; Reguer, S.; Legrand, L., Raman Imaging of Ancient Rust Scales on Archaeological Iron Artefacts for Long-Term Atmospheric Corrosion Mechanisms Study. *J. Raman Spectrosc.* **2006,** *37*, 1228-1237.

54. Biesinger, M. C.; Payne, B. P.; Grosvenor, A. P.; Lau, L. W. M.; Gerson, A. R.; Smart, R. S. C., Resolving Surface Chemical States in XPS Analysis of First Row Transition Metals, Oxides and Hydroxides: Cr, Mn, Fe, Co and Ni. *Appl. Surf. Sci.* **2011,** *257*, 2717-2730.

55. Yang, J.; Liu, H.; Martens, W. N.; Frost, R. L., Synthesis and Characterization of Cobalt Hydroxide, Cobalt Oxyhydroxide, and Cobalt Oxide Nanodiscs. *J. Phys. Chem. C* **2010,** *114*, 111-119.

56. Meini, S.; Solchenbach, S.; Piana, M.; Gasteiger, H. A., The Role of Electrolyte Solvent Stability and Electrolyte Impurities in the Electrooxidation of Li_2O_2 in Li-O_2 Batteries. *J. Electrochem. Soc.* **2014,** *161*, A1306-A1314.

57. Jung, J.; Song, K.; Bae, D. R.; Lee, S. W.; Lee, G.; Kang, Y. M., Beta-FeOOH Nanorod Bundles with Highly Enhanced Round-Trip Efficiency and Extremely Low Overpotential for Llithium-Air Batteries. *Nanoscale* **2013,** *5*, 11845-11849.

58. Lu, J.; Jung Lee, Y.; Luo, X.; Chun Lau, K.; Asadi, M.; Wang, H.-H.; Brombosz, S.; Wen, J.; Zhai, D.; Chen, Z.; Miller, D. J.; Sub Jeong, Y.; Park, J.-B.; Zak Fang, Z.; Kumar, B.; Salehi-Khojin, A.; Sun, Y.-K.; Curtiss, L. A.; Amine, K., A lithium–Oxygen Battery Based on Lithium Superoxide. *Nature* **2016,** *529*, 377-382.

59. Jian, Z.; Liu, P.; Li, F.; He, P.; Guo, X.; Chen, M.; Zhou, H., Core–Shell-Structured $CNT@RuO_2$ Composite as a High-Performance Cathode Catalyst for Rechargeable Li–O_2 Batteries. *Angew. Chem. Int. Ed.* **2014,** *53*, 442-446.

60. Fellinger, T.-P.; Hasché, F.; Strasser, P.; Antonietti, M., Mesoporous Nitrogen-Doped Carbon for the Electrocatalytic Synthesis of Hydrogen Peroxide. *J. Am. Chem. Soc.* **2012,** *134*, 4072-4075.

61. Yang, W.; Fellinger, T.-P.; Antonietti, M., Efficient Metal-Free Oxygen Reduction in Alkaline Medium on High-Surface-Area Mesoporous Nitrogen-Doped Carbons Made from Ionic Liquids and Nucleobases. *J. Am. Chem. Soc.* **2011,** *133*, 206-209.

62. Tsiouvaras, N.; Meini, S.; Buchberger, I.; Gasteiger, H. A., A Novel On-Line Mass Spectrometer Design for the Study of Multiple Charging Cycles of a Li-O_2 Battery. *J. Electrochem. Soc.* **2013,** *160*, A471-A477.

63. Meini, S.; Piana, M.; Tsiouvaras, N.; Garsuch, A.; Gasteiger, H. A., The Effect of Water on the Discharge Capacity of a Non-Catalyzed Carbon Cathode for Li-O_2 Batteries. *Electrochem. Solid St.* **2012,** *15*, A45.

64. Piana, M.; Wandt, J.; Meini, S.; Buchberger, I.; Tsiouvaras, N.; Gasteiger, H. A., Stability of a Pyrrolidinium-Based Ionic Liquid in Li-O_2 Cells. *J. Electrochem. Soc.* **2014,** *161*, A1992-A2001.